Quantized movement of magnetic skyrmions in moiré multiferroic heterostructures

Wei Sun [1], Wenxuan Wang,[1] Changhong Yang,[1,*] Xiaoning Li,[3] Hang Li,[2,4,†] Shifeng Huang,[1,‡] and Zhenxiang Cheng [3,§]

[1]*Shandong Provincial Key Laboratory of Preparation and Measurement of Building Materials, University of Jinan, Jinan 250022, China*

[2]*Institute for Computational Materials Science, School of Physics and Electronics, Henan University, Kaifeng 475004, China*

[3]*Institute for Superconducting & Electronic Materials, Australian Institute of Innovative Materials, University of Wollongong, Innovation Campus, Squires Way, North Wollongong, New South Wales 2500, Australia*

[4]*Institute of Quantum materials and physics, Henan Academy of Sciences, Zhengzhou 450046, China*

(Received 29 November 2022; revised 30 March 2023; accepted 10 May 2023; published 25 May 2023)

Moiré superlattices made with van der Waals layers are an excellent platform for exploring a wide range of exotic and important physical phenomena. In this study, we used first-principles calculations and atomistic spin dynamics simulations to design a two-dimensional van der Waals $MnS_2/CuInP_2S_6$ multiferroic moiré heterosuperlattice with tunable skyrmions through magnetoelectric coupling. The inherent lattice mismatch between the two monolayers of MnS_2 and $CuInP_2S_6$ creates incommensurate moiré patterns, along with modulated magnetic anisotropy and emerging magnetic skyrmions in MnS_2. The magnetic skyrmion in MnS_2 is strongly influenced by magnetoelectric coupling and can be tuned by the ferroelectric polarization of $CuInP_2S_6$. Furthermore, these magnetic skyrmions can be controlled by a pulsed current to move or freeze within the moiré period under different ferroelectric polarization states of the $CuInP_2S_6$ layer. Our work showcases a two-dimensional van der Waals moiré heterosuperlattice with magnetoelectrically tuned magnetic skyrmions, which establishes a foundation for designing future spintronic devices.

DOI: 10.1103/PhysRevB.107.184439

I. INTRODUCTION

Two-dimensional (2D) van der Waals (vdW) materials with strong intralayer coupling but weak interlayer coupling offer an additional "tuning knob" [1–5]. When two or more 2D crystals are superimposed with a relative twist or lattice mismatch between the layers, a moiré superlattice with modulated electronic properties of the heterostructure (HS) emerges, which opens a different research frontier for emerging and intriguing physical phenomena [6,7]. For instance, the spin topology textures of magnetic CrI_3 bilayers [8], Mott insulators in WSe_2/WS_2 moiré superlattices [9,10], and unconventional superconductivity have recently been observed in twisted graphene with small magic angles [11–14]. Moiré superlattice materials can be made of two layers of the same material stacked with a twist angle (homobilayers) or from different materials with a lattice mismatch and without resorting to any twist angle (heterobilayers) [15]. In particular, for moiré heterobilayers, the vast array of 2D vdW crystals can be fully combined with moiré physics, which enjoys structural flexibility, providing a vast range of possibilities for engineering HSs with superior properties [15,16].

Exploring the evolution of the moiré pattern in 2D vdW multiferroic HSs is an exciting topic. The long periodic moiré superlattices offer fertile ground for tuning magnetic properties, including magnetic topological textures, as well as strong magnetoelectric coupling in an atomically thin 2D limit, which can lead to technological advances in a variety of applications such as nonvolatile memories and sensors [8,17–22]. It is important to emphasize that the investigations into the physical phenomena of magnetism in vdW moiré HSs are just becoming a research frontier. Particularly, multiferroic moiré superlattices remain unexplored.

When single layers of 2D magnetic materials are stacked on top of a ferroelectric monolayer with a small lattice mismatch, even a slight lattice mismatch can lead to sustained in-plane lattice displacement, generating a local change in the stacking configurations over a long range. Together with the switchable polarization, this can reconfigure the magnetic anisotropy and Dzyaloshinskii-Moriya interaction (DMI) of the magnetic layers, resulting in spin textures that can be tuned by an electric field [23]. First-principles calculations have shown that different stacking configurations play key roles in determining the magnetic physical properties, such as the magnetism tuning realized with stacking configurations in Fe_3GeTe_2/In_2Se_3 [24] and $CrGeTe_3/In_2Se_3$ [25] HSs. Therefore, more exotic tuning of magnetism by moiré field is highly expected in the multiferroic HS system.

The magnetic skyrmion, a spin texture characterized by topologically protected magnetic and transport properties [26,27], holds promise for next-generation information storage and processing devices, such as racetrack memory [28]. By integrating this magnetic texture into 2D vdW multiferroic moiré HSs and manipulating it with out-of-plane electric polarization of a 2D ferroelectric instead of a tunneling current, energy dissipation of skyrmion-based devices can be effectively reduced [29,30]. Unlike skyrmions usually observed in bilayer moiré lattices constructed with two same 2D vdW magnetic layers, the skyrmion in HSs composed

*Corresponding author: mse_yangch@ujn.edu.cn
†Corresponding author: hang.li@vip.henu.edu.cn
‡Corresponding author: mse_huangsf@ujn.edu.cn
§Corresponding author: cheng@uow.edu.au

of one nonmagnetic layer arises innovatively from the DMI effect introduced from the broken inverse symmetry of the HS. This skyrmion can be easily driven by current and crucially, the ferroelectric layer offers switchable properties in moiré potential, adding an extra degree of tunability to the physical property of the HS. Moreover, the moiré field generated in the HS may cause the skyrmion to move in an ordered potential well, potentially enabling addressability and eliminates the transverse drift of the skyrmion caused by the Hall effect [31].

In this study, we have developed a moiré multiferroic HS by stacking a magnetic 2D vdW single layer of MnS_2 on top of ferroelectric 2D vdW $CuInP_2S_6$, resulting in the emergence of magnetic skyrmions. Using a combination of *ab initio* calculations and micromagnetic simulations, we have demonstrated the modulation of magnetic anisotropy and skyrmions by different polarized states in $MnS_2/CuInP_2S_6$ moiré HS. Moreover, we have found that magnetic skyrmions can be transported quantitatively with periodic steps, driven by pulsed current. In the $P+$ state, Cu ions of $CuInP_2S_6$ layer in the R_0 region move towards the MnS_2 layer, leading to a change in the magnetic easy axis and enabling tunable quantized skyrmion transport in the moiré potential well. Based on these findings, we have designed two pulsed currents to control skyrmion moving, freezing, and direction. This study demonstrates the concept of ME coupled tuning of magnetic skyrmions in a 2D vdW moiré superlattice, laying the foundation for designs of related spintronics devices.

II. METHODS

A. Density functional theory calculation

The magnetic properties and electronic structure of the materials were calculated using first-principles simulations within density functional theory (DFT) [32,33]. The projected augmented wave pseudopotentials method was used as implemented in the Vienna Ab initio Simulation Package (VASP) [34,35]. The exchange correlation energy was calculated using the generalized gradient approximation (GGA) of the Perdew-Burke-Ernzerhof form [36]. A Hubbard U_{eff} parameter of 4 eV was applied to Mn d orbitals using the Dudarev method to correct the strong Coulomb interaction on the $3d$ orbital of the transition metal [37]. The semiempirical DFT-D3 method was used to include the van der Waals interaction, and the plane wave cutoff energy was set to 500 eV [38]. For the calculation of MnS_2 and $CuInP_2S_6$, a centered $18 \times 18 \times 1$ Monkhorst-Pack k-point mesh was used. The plane lattice constant and atomic coordinates were fully relaxed until the energy and force converged to 10^{-5} eV and 10^{-2} eV/Å, respectively, using the conjugate gradient method. The magnetic anisotropy energy (MAE) was determine using a high energy convergence standard of 10^{-6} eV and spin-orbit coupling. To eliminate the periodic boundary effect, the vacuum space between adjacent slabs was set to be larger than 15 Å along the z direction. For more details, please refer to part 1 of the Supplemental Material [39] (see also Refs. [40,41] therein).

Before analyzing the effective magnetic Hamiltonian, we will describe the configuration of our HSs. The $1T$-MnS_2 monolayer has a space group of $P\bar{3}1m$ with a Mn-S-Mn bond angle of $\sim 90^\circ$, and it exhibits intralayer ferromagnetic ordering through the Mn-S-Mn superexchange interaction. The $CuInP_2S_6$ ferroelectric monolayer has a $P3$ space group and switchable spontaneous out-of-plane polarization resulting from the relative displacement of Cu ions along the z axis. The polarized state is referred to as $P+$ when the Cu atom is close to the upper surface and $P-$ when it flips over. To better match the $CuInP_2S_6$ lattice, we used a $\sqrt{3} \times \sqrt{3}$ MnS_2 supercell for calculations with DFT-calculated lattice constants of 3.43 Å for MnS_2 and 6.08 Å for $CuInP_2S_6$ monolayers. Due to the lattice mismatch of $\delta = 0.02$, the stacked bilayers of 2D MnS_2 and $CuInP_2S_6$ form the period moiré HS, in which the stacking order in each local region R closely resembles the lattice-matched stacking configuration but changes smoothly over a long range. The moiré periodicity, shown in Fig. 1(a), is approximately $A \approx a/\sqrt{\delta^2 + \theta^2}$ for a small lattice mismatch δ and/or twisting angle θ, where a is the lattice constant of the MnS_2 monolayer. The moiré periodicity A can be further tuned with a relative twisting between the layers. For the $MnS_2/CuInP_2S_6$ moiré HS, the stacking order in any local region in the moiré pattern can be obtained by translating the MnS_2 monolayer with the vector $r = \eta a_1 + \nu a_2$, where η, $\nu \in [0, [1]]$, and a_1 and a_2 are the lattice vectors of the MnS_2 unit cell. In one moiré period, the local region R_0, R_1, R_2 stacking configuration corresponds to the MnS_2 shift $r = (a_1 + a_2,\ \frac{1}{3}a_1 + \frac{2}{3}a_2,\ \frac{2}{3}a_1 + \frac{1}{3}a_2)$ with respect to $CuInP_2S_6$, as shown in Fig. 1(b).

To determine the magnetic properties of a moiré pattern, it is challenging to directly calculate them due to the large number of atoms involved, which is proportional to $(A/a)^2$. Therefore, we follow the method outlined in Refs. [8,42] to derive the effective magnetic physical parameters in moiré HS. The exchange constant and magnetic anisotropy were parametrized by evaluating the energy on a 6×6 grid of points for a moiré HS, where MnS_2 was shifted relative to $CuInP_2S_6$ in the unit cell to sample the entire moiré range. Each grid point corresponded to a lateral shift $r = (\frac{i}{6}a_1 + \frac{j}{6}a_2)$ for $i, j = 0$–6 along the crystalline axes. We then interpolate these data by fitting to a polynomial to obtain the magnetic physical parameters for the entire moiré HS. To ensure that the lateral shift vector $\boldsymbol{r}$ remained unchanged during structural relaxation, we fixed the in-plane positions of all atoms in the bilayer but allowed them to relax in the out-of-plane direction.

B. Atomistic spin dynamics simulations

Based on the magnetic parameters derived above, we used the SPIRIT package to simulate the steady state and dynamics of the magnetization textures [43]. The time evolution of the magnetization is described by the Landau-Lifshitz-Gilbert (LLG) equation [44,45], which can be written as

$$\begin{aligned}\frac{\partial \mathbf{m}_i}{\partial t} = &-\frac{\gamma}{(1+\alpha^2)\mu_i}\mathbf{m}_i \times \mathbf{B}_i^{\text{eff}}(t) - \frac{\gamma\alpha}{(1+\alpha^2)\mu_i}\mathbf{m}_i \\ &\times \left[\mathbf{m}_i \times \mathbf{B}_i^{\text{eff}}(t)\right] - \frac{\alpha-\beta}{(1+\alpha^2)}u\mathbf{m}_i \times (\hat{\mathbf{j}}\cdot\nabla)\mathbf{m}_i \\ &+ \frac{1+\beta\alpha}{(1+\alpha^2)}u\mathbf{m}_i \times [\mathbf{m}_i \times (\hat{\mathbf{j}}\cdot\nabla)\mathbf{m}_i]. \end{aligned} \quad (1)$$

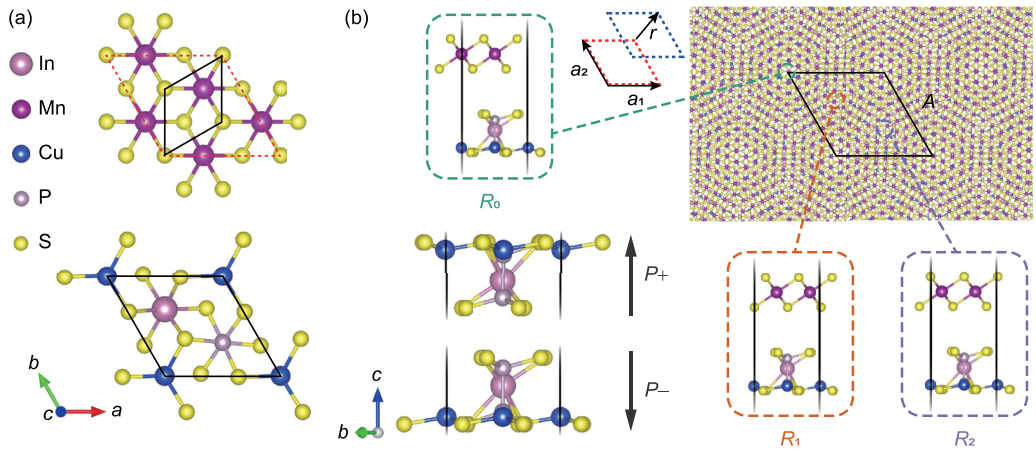

FIG. 1. (a) Top and (b) side views of a moiré HS. Three local regions R_0, R_1, and R_2 of the stacking configurations are amplified to show their different interlayer configurations in the moiré superlattice.

Here, γ is the electron gyromagnetic ratio, $\alpha = 0.05$ is the damping parameter, and $\beta = 0.01$ is a nonadiabaticity parameter. The term u is defined as $jPg\mu_B/(2eM_s)$, where j is the current density, P is the polarization of the current, e is the electron charge, and M_s is the saturation magnetization. The vector $\hat{\mathbf{j}} = x$ denotes the electron current normal vector, and $\nabla = \partial/\partial r$ is the spatial gradient acting on the spin orientation.

III. RESULTS

Figure 2 displays the exchange interactions and single-ion anisotropy energy of the MnS_2 section in the moiré patterns. According to the Goodenough-Kanamori-Anderson rule, ferromagnetic superexchange interactions remain stable regardless of interlayer stacking configuration and polarization directions, as long as the Mn-S-Mn bonds of the MnS_2 system are near 90° [46–48]. Therefore, the exchange interaction value remains between 1.9 and 2.1 meV for both upward and downward polarized states, as shown in Figs. 2(a) and 2(b). The relatively large value is evident in the R_0 region as well. However, as illustrated in Figs. 2(c) and 2(d), the single-ion anisotropy is closely linked to the interlayer stacking configuration. Particularly interesting are situations in which the easy axis's direction changes from in-plane to out-of-plane near the R_1 region in the $P+$ state, resulting in an effective moiré field that weakens significantly after polarization reversal. Thus, stacking-related anisotropy generates a prominent local difference over a long period, but it can be freely shifted between in plane and out of plane by the external electric field-induced switching of polarization states. This capability opens interesting opportunities for developing 2D vdW multiferroic HSs.

To simulate the magnetization texture in a moiré field, we utilized a $2A \times 2A$ supercell with periodic boundaries and employed the LLG equation [44,45]. The atomic effective

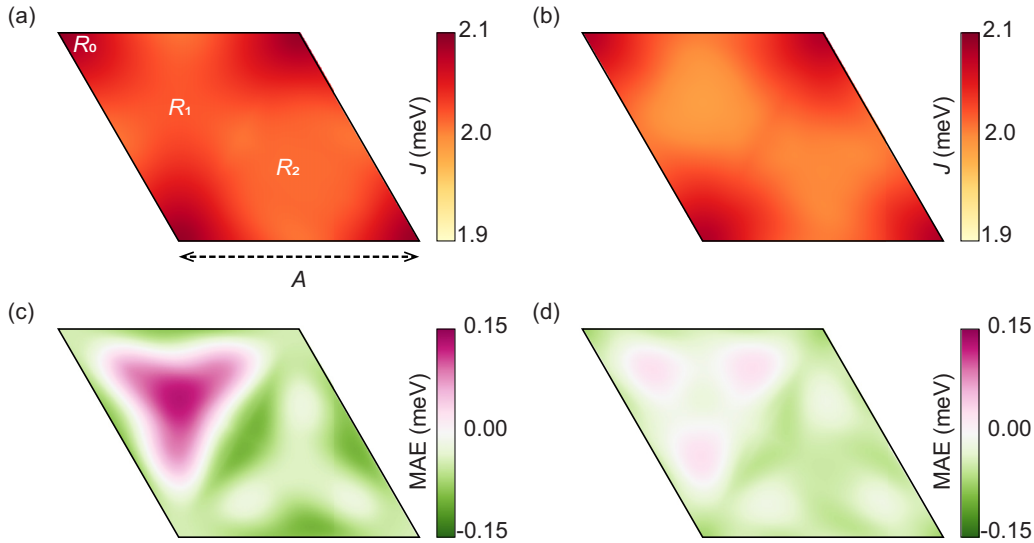

FIG. 2. Panels (a) and (b) represent the magnetic exchange interaction texture, and (c) and (d) indicate the MAE texture in the Moiré HS under the $P+$ and $P-$ states, respectively.

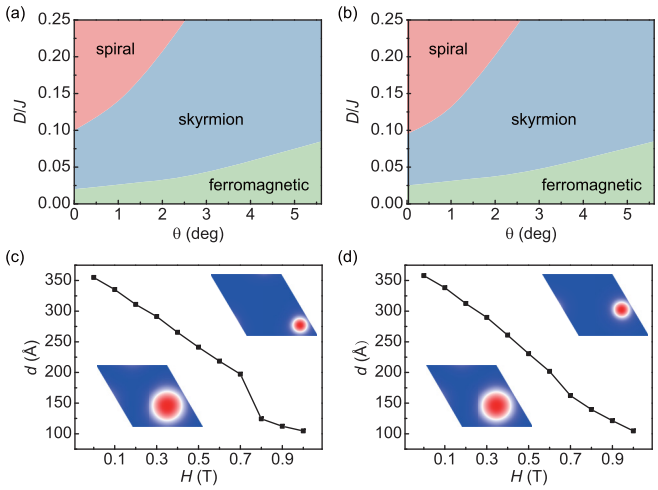

FIG. 3. Panels (a) and (b) represent the phase diagrams in the $P+$ and $P-$ states as a function of θ-dependent magnetic texture and D/J. Panels (c) and (d) are the skyrmion diameter in the $P+$ and $P-$ states as a function of magnetic field, respectively.

Hamiltonian of MnS_2 was written as follows:

$$H = -\sum_i \mathbf{B}\cdot\mathbf{m}_i - \sum_{\langle i,j\rangle} J(\mathbf{r}_{ij})\mathbf{m}_i\cdot\mathbf{m}_j - \sum_i K(\mathbf{r}_{ij})(\mathbf{m}_i\cdot\hat{\mathbf{z}})^2 - \sum_{\langle i,j\rangle}\mathbf{D}(\mathbf{r}_{ij})\cdot(\mathbf{m}_i\times\mathbf{m}_j). \quad (2)$$

Here, $\mathbf{m}_i$ is the magnetic moment at the ith Mn site, and $\langle ij\rangle$ denotes that sites i and j are nearest neighbors. $\mathbf{B}$ represents the external magnetic field, where J and K are the exchange interaction and single-ion anisotropy, respectively, and both of which are functions of the interlayer relative displacement $\mathbf{r}_{ij}$ in Fig. 2. We denote $\mathbf{D}$ as the DMI, which can arise from the symmetry breaking of heterostructures. We have conducted DMI calculations for the R_0 region and have summarized the magnetic parameters, as shown in Table SI of the Supplemental Material [39]. It is worth noting that experiments have confirmed that DMI can be adjusted by using different heavy metal substrates or via liquid ion gating [49–51]. Therefore, we have introduced DMI as a variable in our atomistic spin dynamics simulations. Moreover, since the moiré periodicity A can be modulated by the twist angle θ between layers, we depicted the phase diagram as a function of the θ-dependent magnetic texture and D/J, as demonstrated in Figs. 3(a) and 3(b).

Next, we choose a moiré HS with $D/J = 0.05$ and no twisting angle ($A \approx 50a$) to investigate the effects of an external magnetic field on skyrmions with two polarization states (see part 2 of the Supplemental Material [39] for details on the spin texture). The insets in Figs. 3(c) and 3(d) show the skyrmion configurations with the magnetic field near 0.5 and 0.9 T, respectively. An abrupt change in the skyrmion diameter and accompanying location excursion emerged near 0.7 T, which was particularly noticeable for the $P+$ state. This change can be attributed to two main causes: (1) easy magnetic axis reversal introduces a larger energy potential barrier at the local R_1 region with a $P+$-polarized state, and (2) the perpendicular magnetic anisotropy is able to host the spin texture of a skyrmion core, pinning the relatively large skyrmion at the center of the R_1 region. As the radius decreases, shrinking of the edge of the skyrmion with in-plane spin texture raises the energy levels in the R_1 region and eventually enables the skyrmion to slide towards the lower energy region.

The switchable potential arises from the tunable magnetic easy axis in the R_1 region, while retaining in-plane magnetic anisotropy in the R_0 and R_2 regions. This strongly suggests that local interlayer stacking, which depends on the moiré lattice mismatch, plays a crucial role in determining the final properties. Two stacking configurations, R_0 and R_1, were considered in the $P+$ state, which give rise to the distinct Cu ion distribution shown schematically in Fig. 4(a). In the freestanding $CuInP_2S_6$ monolayer and the $CuInP_2S_6$ part of the HS in the R_0 region, Cu ions are located in the interior of the framework composed of S ions. For the R_1 region, this $P+$ configuration drives Cu ions towards the MnS_2 layer. Actually, a uniaxial quadruple potential well caused by the Cu ion distance has been experimentally observed for the $CuInP_2S_6$ multilayer system [52]. This is in sharp contrast to our spontaneously formed triple potential well resulting from different stacking configurations in the $MnS_2/CuInP_2S_6$ HS. It should be noted that our different potential scale is primarily due to the consistent distribution of Cu ions, which leads to unified polarization in the R_0 and R_1 regions under the $P-$ state.

In the maximally localized Wannier orbitals [53], a strong orbital overlap between the Cu-d and Mn-d orbitals through intermediate S ions is observed after the Cu ions extend beyond the van der Waals gap in the R_1 region, as schematically shown in Fig. 4(a). The orbital-projected density of states (DOS) in Fig. 4(b) demonstrates the orbitals' hybridization between Cu-d and Mn-d states in the energy range 0–1.5 eV, resulting in the generation of magnetic moment $m_{Cu} = 0.1\ \mu_B$ accompanied by out-of-plane magnetic anisotropy, as shown in Fig. 4(c). This suggests that Cu ion spin-orbit coupling plays a major role in MAE. In contrast, in the R_0 region, the vdW gap prevents the orbit overlap scenario and makes the contribution of Cu ions to the MAE negligible. Therefore, the reversal of the easy magnetic axis from in plane to out of plane in the R_1 region has emerged as a direct result of Cu displacement-related orbital interactions, as shown in Figs. 4(a)–4(c).

In the R_1 region, the out-of-plane anisotropy is dominated by Cu-d orbitals, while the Mn-d orbitals contribute a negative MAE. This can be explained using a second-order perturbation theory [54], where the MAE is described as

$$\mathrm{MAE} = \sum_{\sigma\sigma'} E^{\sigma\sigma'}(x) - E^{\sigma\sigma'}(z) = \sum_{\sigma\sigma'}(2\delta_{\sigma\sigma'} - 1)\xi^2 \times \sum_{o^\sigma u^{\sigma'}} \frac{|\langle o^\sigma|L_z|u^{\sigma'}\rangle|^2 - |\langle o^\sigma|L_x|u^{\sigma'}\rangle|^2}{E_u^{\sigma'} - E_o^\sigma}, \quad (3)$$

where ξ represents the SOC constant and $E_u^{\sigma'}$ and E_o^σ are the energy levels of the unoccupied states with spin σ' and occupied states with spin σ, respectively, for the magnetization along the x [100] and z [001] directions. The difference in the square of the angular momentum

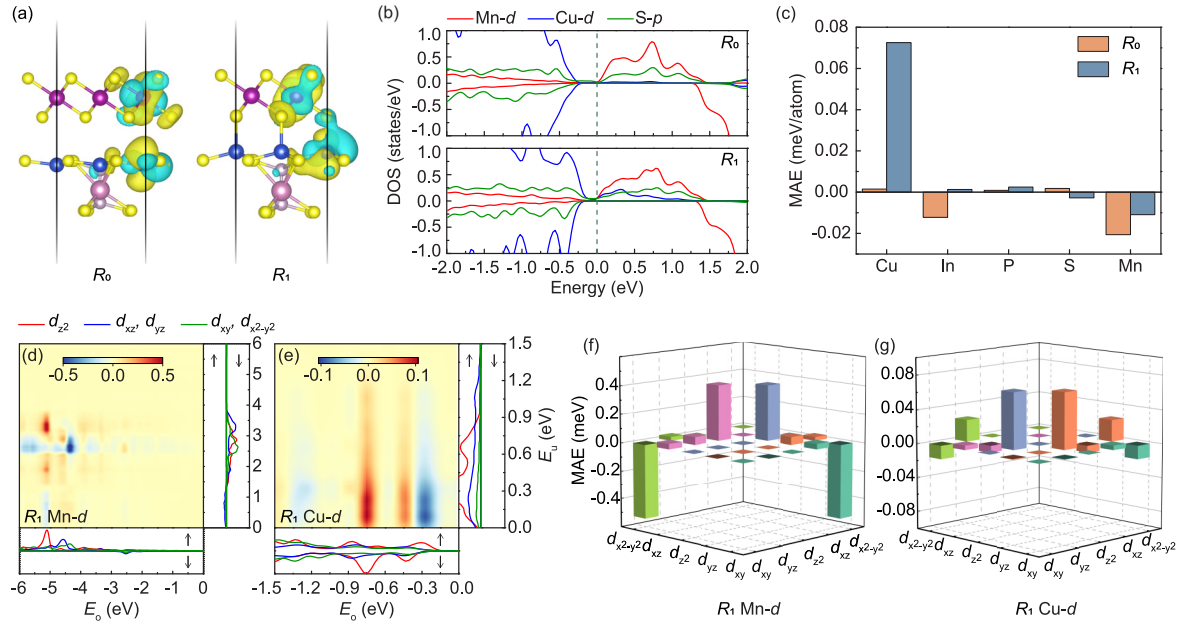

FIG. 4. (a) The d-orbital Wannier function in the R_0 and R_1 regions under the $P+$ state, where the isosurface is set to ± 2 Å$^{-3/2}$. (b) The orbital-projected DOS and (c) atom-resolved MAE in the R_0 and R_1 regions. Panels (d) and (e) are the MAE(E_o, E_u) density of Mn-d and Cu-d states in the R_1 region, respectively. Panels (f) and (g) shown the d-orbital-resolved MAEs of Mn and Cu atoms in the R_1 region, respectively.

matrix element for the two magnetization directions $(2\delta_{\sigma\sigma'}-1)(|\langle o^{\sigma}|L_z|u^{\sigma'}\rangle|^2-|\langle o^{\sigma}|L_x|u^{\sigma'}\rangle|^2)$ is simplified as the matrix element difference in Table I.

According to Eq. (3), the MAE primarily arises from the hybridization between occupied and unoccupied electronic states through SOC. Therefore, we computed the MAE(E_o, E_u) density for Mn-d and Cu-d orbitals in the R_1 region, along with occupied and unoccupied densities of states. However, we ignored the SOC constant ξ as it acts only as an overall scaling factor. For Mn-d orbitals, Fig. 4(d) displays a strong negative peak near ($E_o=-4.5$, $E_u=2.5$), which, combined with the results listed in Table I, results from the interaction of spin-up occupied states (d^{o+}_{xy}, $d^{o+}_{x^2-y^2}$) and spin-down unoccupied states (d^{u-}_{xy}, $d^{u-}_{x^2-y^2}$). Moreover, a substrong positive peak appears near ($E_o=-5.2$, $E_u=3.4$) from the interaction of spin-up occupied states ($d^{o+}_{z^2}$) and spin-down unoccupied states (d^{u-}_{yz}). Integrating the MAE density, we find that Mn-d orbitals contribute a weak negative MAE. In contrast, the contribution of Cu-d orbitals to MAE mainly arises from the interaction of occupied states ($d^{o+}_{z^2}$, $d^{o-}_{z^2}$) and spin-up unoccupied states (d^{u+}_{yz}). Among them, $d^{o-}_{z^2}$ states

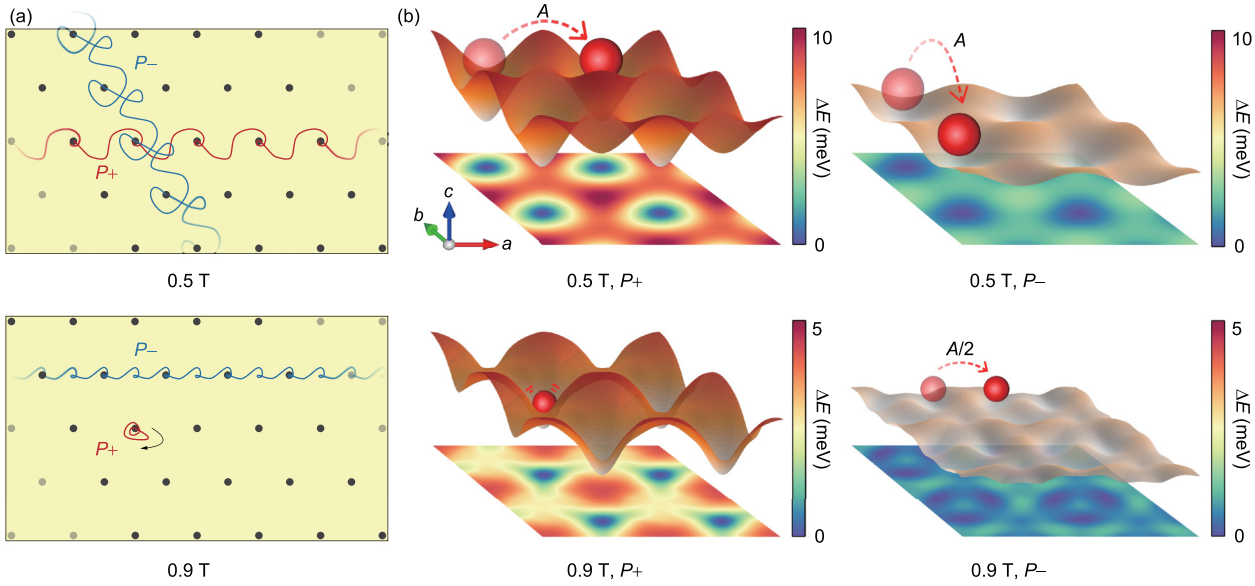

FIG. 5. (a) Trajectory of skyrmions in the moiré field under different polarization states. (b) Schematic diagram of the motion of skyrmions in superlattice potentials under different external conditions.

TABLE I. Matrix differences between magnetization along z [001] and x [100] in Eq. (3). o and u represent occupied states and unoccupied states, respectively.

	$\sigma = \sigma'$					$\sigma = -\sigma'$				
	d^u_{xy}	d^u_{yz}	$d^u_{z^2}$	d^u_{xz}	$d^u_{x^2-y^2}$	d^u_{xy}	d^u_{yz}	$d^u_{z^2}$	d^u_{xz}	$d^u_{x^2-y^2}$
d^o_{xy}	0	0	0	−1	4	0	0	0	1	−4
d^o_{yz}	0	0	−3	1	−1	0	0	3	−1	1
$d^o_{z^2}$	0	−3	0	0	0	0	3	0	0	0
d^o_{xz}	−1	1	0	0	0	1	−1	0	0	0
$d^o_{x^2-y^2}$	4	−1	0	0	0	−4	1	0	0	0

contribute a positive peak near $E_o = -0.75$ and -0.4 eV, and $d^{o+}_{z^2}$ states contribute a negative peak near $E_o = -0.2$, as shown in Fig. 4(e). Finally, the total MAE indicates an easy-axis magnet dominated by Cu-d orbitals. These results are consistent with the d-orbital-resolved MAE of the Mn and Cu atoms displayed in Figs. 4(f) and 4(g), indicating the conclusion's reliability. In the R_0 region, since the unoccupied states of Cu-d orbitals near the Fermi level are empty, according to Eq. (3), the contribution of Cu ions to the MAE is almost negligible. Therefore, the total MAE is an easy plane magnet dominated by Mn-d orbitals. Refer to part 3 of the Supplemental Material [39] for MAE density and orbital-resolved MAE in the R_0 region.

In light of the successful modulation of localized easy magnetic axes in moiré HSs, we propose a strategy for quantized transportation of skyrmions driven by electric polarization switching. Since there is an abrupt change in the skyrmion pattern with a magnetic field near 0.7 T, we considered the scenario of 0.5 and 0.9 T to fully relax the structure within a $4A \times 4A$ supercell for a single skyrmion. We also tested in a $5A \times 5A$ supercell to avoid the artifacts due to periodic boundaries (see the part 4 of the Supplemental Material [39]). As outlined in Fig. 5(a), we employed a spin transfer torque of magnitude $u = jP\hbar\mu_B/(2eM_s) = 0.01$ meV and a width of 60 ps to simulate the in-plane current pulses. As a result, skyrmions moved more smoothly in the moiré field under the $P-$ state compared with their $P+$ counterparts when uniform current injection was provided. Specifically, under a 0.5-T magnetic field, skyrmions traveled orderly along the [100] direction with a step size of A upon $P-$ state; when switching to the upwards polarized state, the move path is transformed to the $[\bar{1}00]$ direction and the step size is kept constant. Surprisingly, at a 0.9-T magnetic field under the $P+$ state, skyrmions were trapped in a potential well and could not be transferred to another well by current driving. In contrast, in the $P-$ state at 0.9 T, skyrmions experienced a change in movement with steps of $A/2$. In addition, we also confirmed the influence of different amplitudes and directions of current on the quantized transportation of skyrmions driven (see part 5 of the Supplemental Material [39]); this suggested the possibility of tuning the moving step distance and moving direction of the skyrmion by electric field control of ferroelectric polarization approaches, and even movement and freezing of the skyrmion can be controlled.

We calculated the moiré potential including the four energies described in Eq. (2), within a $2A \times 2A$ supercell, as illustrated in Fig. 5(b). It is evident that the flatter potential field allowed for smoother driving of skyrmions by the current pulse in the $P-$ state compared to the $P+$ state, despite the same external magnetic field. Moreover, since the current-driven skyrmion moves periodically between highly organized moiré potential wells, the disadvantage of transverse drift caused by the Hall effect can be minimized during current injection. Furthermore, the platform of the moiré lattice allows for the realization of electric field tunable quantum transport of skyrmions [8,55,56].

IV. CONCLUSION

In conclusion, our first-principles calculation has showed that a slight mismatch between the stacked layers in a MnS_2/$CuInP_2S_6$ vdW HS generates moiré superlattice patterns, which have a significant impact on the magnetic anisotropy and magnetic skyrmion of MnS_2, and can be controlled by two ferroelectric polarization states. We have also investigated the effect of different polarized states on magnetic texturing of the MnS_2, combining *ab initio* calculations with a micromagnetic simulation approach. Our proposed approach for pulsed current-driven skyrmion transport allows for the control of skyrmion movement or freezing within the moiré period by applying different ferroelectric polarizations, demonstrating the interesting physical property of tunability/controllability in the moiré superlattice.

ACKNOWLEDGMENTS

This work was supported by the National Natural Science Foundation of China (Grants No. 51972144, No. 52102238, and No. U1806221), the Taishan Scholars Program, the Case-by-Case Project for Top Outstanding Talents of Jinan, the Shandong Provincial Natural Science Foundation (Grant No. ZR2020KA003), the Project of "20 Items of University" of Jinan (Grants No. T202009 and No. T201907), and the Shandong Provincial Key Research and Development Plan (Grant No. 2022CXPT045). H.L. acknowledges the support from the National Natural Science Foundation of China (Grant No. 11804078) and Henan University (Grant No. CJ3050A0240050). Z.X. Cheng thanks Australia Research Council for support (Grant No. DP190100150).

The authors declare no conflict of interest.

[1] J. L. Lado, Putting a twist on spintronics, Science **374**, 1048 (2021).

[2] M. R. Calvo and C. Rubio-Verdú, New moiré landscapes for atomic spins, Physics **14**, 165 (2021).

[3] A. K. Geim and I. V. Grigorieva, Van der Waals heterostructures, Nature (London) **499**, 419 (2013).

[4] K. Novoselov, A. Mishchenko, A. Carvalho, and A. H. Castro Neto, 2D materials and van der Waals heterostructures, Science **353**, aac9439 (2016).

[5] Y. Liu, N. O. Weiss, X. Duan, H.-C. Cheng, Y. Huang, and X. Duan, Van der Waals heterostructures and devices, Nat. Rev. Mater. **1**, 16042 (2016).

[6] E. Y. Andrei and A. H. MacDonald, Graphene bilayers with a twist, Nat. Mater. **19**, 1265 (2020).

[7] L. Balents, C. R. Dean, D. K. Efetov, and A. F. Young, Superconductivity and strong correlations in moiré flat bands, Nat. Phys. **16**, 725 (2020).

[8] M. Akram, H. LaBollita, D. Dey, J. Kapeghian, O. Erten, and A. S. Botana, Moiré skyrmions and chiral magnetic phases in twisted CrX_3 (X = I, Br, and Cl) bilayers, Nano Lett. **21**, 6633 (2021).

[9] E. C. Regan, D. Wang, C. Jin, M. I. Bakti Utama, B. Gao, X. Wei, S. Zhao, W. Zhao, Z. Zhang, and K. Yumigeta, Mott and generalized Wigner crystal states in WSe_2/WS_2 moiré superlattices, Nature (London) **579**, 359 (2020).

[10] Y. Tang, L. Li, T. Li, Y. Xu, S. Liu, K. Barmak, K. Watanabe, T. Taniguchi, A. H. MacDonald, and J. Shan, Simulation of Hubbard model physics in WSe_2/WS_2 moiré superlattices, Nature (London) **579**, 353 (2020).

[11] Y. Cao, V. Fatemi, S. Fang, K. Watanabe, T. Taniguchi, E. Kaxiras, and P. Jarillo-Herrero, Unconventional superconductivity in magic-angle graphene superlattices, Nature (London) **556**, 43 (2018).

[12] M. Yankowitz, S. Chen, H. Polshyn, Y. Zhang, K. Watanabe, T. Taniguchi, D. Graf, A. F. Young, and C. R. Dean, Tuning superconductivity in twisted bilayer graphene, Science **363**, 1059 (2019).

[13] X. Lu, P. Stepanov, W. Yang, M. Xie, M. A. Aamir, I. Das, C. Urgell, K. Watanabe, T. Taniguchi, and G. Zhang, Superconductors, orbital magnets and correlated states in magic-angle bilayer graphene, Nature (London) **574**, 653 (2019).

[14] G. Chen, A. L. Sharpe, P. Gallagher, I. T. Rosen, E. J. Fox, L. Jiang, B. Lyu, H. Li, K. Watanabe, and T. Taniguchi, Signatures of tunable superconductivity in a trilayer graphene moiré superlattice, Nature (London) **572**, 215 (2019).

[15] E. Y. Andrei, D. K. Efetov, P. Jarillo-Herrero, A. H. MacDonald, K. F. Mak, T. Senthil, E. Tutuc, A. Yazdani, and A. F. Young, The marvels of moiré materials, Nat. Rev. Mater. **6**, 201 (2021).

[16] M. Brzhezinskaya, O. Kononenko, V. Matveev, A. Zotov, I. I. Khodos, V. Levashov, V. Volkov, S. I. Bozhko, S. V. Chekmazov, and D. Roshchupkin, Engineering of numerous moire superlattices in twisted multilayer graphene for twistronics and straintronics applications, ACS nano **15**, 12358 (2021).

[17] C. R. Dean, L. Wang, P. Maher, C. Forsythe, F. Ghahari, Y. Gao, J. Katoch, M. Ishigami, P. Moon, and M. Koshino, Hofstadter's butterfly and the fractal quantum Hall effect in moiré superlattices, Nature (London) **497**, 598 (2013).

[18] L. Ponomarenko, R. Gorbachev, G. Yu, D. Elias, R. Jalil, A. Patel, A. Mishchenko, A. Mayorov, C. Woods, and J. Wallbank, Cloning of Dirac fermions in graphene superlattices, Nature (London) **497**, 594 (2013).

[19] B. Hunt, J. D. Sanchez-Yamagishi, A. F. Young, M. Yankowitz, B. J. LeRoy, K. Watanabe, T. Taniguchi, P. Moon, M. Koshino, and P. Jarillo-Herrero, Massive Dirac fermions and Hofstadter butterfly in a van der Waals heterostructure, Science **340**, 1427 (2013).

[20] C. Gong, L. Li, Z. Li, H. Ji, A. Stern, Y. Xia, T. Cao, W. Bao, C. Wang, and Y. Wang, Discovery of intrinsic ferromagnetism in two-dimensional van der Waals crystals, Nature (London) **546**, 265 (2017).

[21] B. Huang, G. Clark, E. Navarro-Moratalla, D. R. Klein, R. Cheng, K. L. Seyler, D. Zhong, E. Schmidgall, M. A. McGuire, and D. H. Cobden, Layer-dependent ferromagnetism in a van der Waals crystal down to the monolayer limit, Nature (London) **546**, 270 (2017).

[22] F. Xiao, K. Chen, and Q. Tong, Magnetization textures in twisted bilayer CrX_3 (X = Br, I), Phys. Rev. Res. **3**, 013027 (2021).

[23] N. Sivadas, S. Okamoto, X. Xu, C. J. Fennie, and D. Xiao, Stacking-dependent magnetism in bilayer CrI_3, Nano Lett. **18**, 7658 (2018).

[24] L. Yin and D. S. Parker, Out-of-plane magnetic anisotropy engineered via band distortion in two-dimensional materials, Phys. Rev. B **102**, 054441 (2020).

[25] C. Gong, E. M. Kim, Y. Wang, G. Lee, and X. Zhang, Multiferroicity in atomic van der Waals heterostructures, Nat. Commun. **10**, 1 (2019).

[26] U. K. Roessler, A. Bogdanov, and C. Pfleiderer, Spontaneous skyrmion ground states in magnetic metals, Nature (London) **442**, 797 (2006).

[27] S. Mühlbauer, B. Binz, F. Jonietz, C. Pfleiderer, A. Rosch, A. Neubauer, R. Georgii, and P. Böni, Skyrmion lattice in a chiral magnet, Science **323**, 915 (2009).

[28] A. Fert, V. Cros, and J. Sampaio, Skyrmions on the track, Nat. Nanotechnol. **8**, 152 (2013).

[29] W. Sun, W. Wang, H. Li, G. Zhang, D. Chen, J. Wang, and Z. Cheng, Controlling bimerons as skyrmion analogues by ferroelectric polarization in 2D van der Waals multiferroic heterostructures, Nat. Commun. **11**, 1 (2020).

[30] C.-K. Li, X.-P. Yao, and G. Chen, Writing and deleting skyrmions with electric fields in a multiferroic heterostructure, Phys. Rev. Res. **3**, L012026 (2021).

[31] Q. Tong, F. Liu, J. Xiao, and W. Yao, Skyrmions in the Moiré of van der Waals 2D Magnets, Nano Lett. **18**, 7194 (2018).

[32] P. Hohenberg and W. Kohn, Inhomogeneous electron gas, Phys. Rev. **136**, B864 (1964).

[33] W. Kohn and L. J. Sham, Self-consistent equations including exchange and correlation effects, Phys. Rev. **140**, A1133 (1965).

[34] G. Kresse and J. Hafner, *Ab initio* molecular dynamics for liquid metals, Phys. Rev. B **47**, 558 (1993).

[35] G. Kresse and J. Furthmüller, Efficient iterative schemes for *ab initio* total-energy calculations using a plane-wave basis set, Phys. Rev. B **54**, 11169 (1996).

[36] J. P. Perdew, K. Burke, and M. Ernzerhof, Generalized Gradient Approximation made Simple, Phys. Rev. Lett. **77**, 3865 (1996).

[37] S. L. Dudarev, G. A. Botton, S. Y. Savrasov, C. J. Humphreys, and A. P. Sutton, Electron-energy-loss spectra and the structural stability of nickel oxide: An LSDA+U study, Phys. Rev. B **57**, 1505 (1998).

[38] S. Grimme, J. Antony, S. Ehrlich, and H. Krieg, A consistent and accurate *ab initio* parametrization of density functional dispersion correction (DFT-D) for the 94 elements H-Pu, J. Chem. Phys. **132**, 154104 (2010).

[39] See Supplemental Material at http://link.aps.org/supplemental/10.1103/PhysRevB.107.184439 for more information about the detailed methods and data discussion.

[40] H. Xiang, E. Kan, S.-H. Wei, M.-H. Whangbo, and X. Gong, Predicting the spin-lattice order of frustrated systems from first principles, Phys. Rev. B **84**, 224429 (2011).

[41] H. Yang, A. Thiaville, S. Rohart, A. Fert, and M. Chshiev, Anatomy of Dzyaloshinskii-Moriya Interaction at Co/Pt Interfaces, Phys. Rev. Lett. **115**, 267210 (2015).

[42] S. Carr, D. Massatt, S. B. Torrisi, P. Cazeaux, M. Luskin, and E. Kaxiras, Relaxation and domain formation in incommensurate two-dimensional heterostructures, Phys. Rev. B **98**, 224102 (2018).

[43] G. P. Müller, M. Hoffmann, C. Dißelkamp, D. Schürhoff, S. Mavros, M. Sallermann, N. S. Kiselev, H. Jónsson, and S. Blügel, Spirit: Multifunctional framework for atomistic spin simulations, Phys. Rev. B **99**, 224414 (2019).

[44] L. Landau and E. Lifshitz, in *Perspectives in Theoretical Physics* (Elsevier, New York, 1992), pp. 51–65.

[45] T. L. Gilbert, A phenomenological theory of damping in ferromagnetic materials, IEEE Trans. Magn. **40**, 3443 (2004).

[46] J. Kanamori, Crystal distortion in magnetic compounds, J. Appl. Phys. **31**, S14 (1960).

[47] J. B. Goodenough, Theory of the role of covalence in the perovskite-type manganites [La, M (II)]MnO_3, Phys. Rev. **100**, 564 (1955).

[48] P. W. Anderson, New approach to the theory of superexchange interactions, Phys. Rev. **115**, 2 (1959).

[49] L. Herrera Diez, Y. Liu, D. A. Gilbert, M. Belmeguenai, J. Vogel, S. Pizzini, E. Martinez, A. Lamperti, J. Mohammedi, and A. Laborieux, Nonvolatile Ionic Modification of The Dzyaloshinskii-Moriya Interaction, Phys. Rev. Appl. **12**, 034005 (2019).

[50] W. Sun, W. Wang, J. Zang, H. Li, G. Zhang, J. Wang, and Z. Cheng, Manipulation of magnetic skyrmion in a 2D van der Waals heterostructure via both electric and magnetic fields, Adv. Funct. Mater. **31**, 2104452 (2021).

[51] Y. Wu, S. Zhang, J. Zhang, W. Wang, Y. L. Zhu, J. Hu, G. Yin, K. Wong, C. Fang, and C. Wan, Néel-type skyrmion in WTe_2/Fe_3GeTe_2 van der Waals heterostructure, Nat. Commun. **11**, 3860 (2020).

[52] J. A. Brehm, S. M. Neumayer, L. Tao, A. O'Hara, M. Chyasnavichus, M. A. Susner, M. A. McGuire, S. V. Kalinin, S. Jesse, and P. Ganesh, Tunable quadruple-well ferroelectric van der Waals crystals, Nat. Mater. **19**, 43 (2020).

[53] N. Marzari, A. A. Mostofi, J. R. Yates, I. Souza, and D. Vanderbilt, Maximally localized Wannier functions: Theory and applications, Rev. Mod. Phys. **84**, 1419 (2012).

[54] D. S. Wang, R. Wu, and A. J. Freeman, First-principles theory of surface magnetocrystalline anisotropy and the diatomic-pair model, Phys. Rev. B **47**, 14932 (1993).

[55] C. Reichhardt, D. Ray, and C. J. Olson Reichhardt, Quantized transport for a skyrmion moving on a two-dimensional periodic substrate, Phys. Rev. B **91**, 104426 (2015).

[56] W. Wang, D. Song, W. Wei, P. Nan, S. Zhang, B. Ge, M. Tian, J. Zang, and H. Du, Electrical manipulation of skyrmions in a chiral magnet, Nat. Commun. **13**, 1593 (2022).